

EMBEDDED INFRARED FIBER OPTIC
ABSORPTION STUDIES OF
NITRAMINE PROPELLANT
STRAND BURNING

Final Report

19950203 169

REPORT DOCUMENTATION PAGE

Form Approved
OMB No. 0704-0188

Public reporting burden for this collection of information is estimated to average 1 hour per response, including the time for reviewing instructions, searching existing data sources, gathering and maintaining the data needed, and completing and reviewing the collection of information. Send comments regarding this burden estimate or any other aspect of this collection of information, including suggestions for reducing this burden, to Washington Headquarters Services, Directorate for Information Operations and Reports, 1215 Jefferson Davis Highway, Suite 1204, Arlington, VA 22202-4302, and to the Office of Management and Budget, Paperwork Reduction Project (0704-0188), Washington, DC 20503.

1. AGENCY USE ONLY (Leave blank)		2. REPORT DATE 4 November 1994		3. REPORT TYPE AND DATES COVERED Final Report, 9/5/93-9/5/94	
4. TITLE AND SUBTITLE Embedded Infrared Fiber Optic Absorption Studies of Nitramine Propellant Strand Burning				5. FUNDING NUMBERS DAAH04-93-C-0053	
6. AUTHOR(S) J. Wormhoudt, P. L. Kebabian, and C. E. Kolb					
7. PERFORMING ORGANIZATION NAME(S) AND ADDRESS(ES) Aerodyne Research, Inc. 45 Manning Road Billerica, MA 01821				8. PERFORMING ORGANIZATION REPORT NUMBER	
9. SPONSORING/MONITORING AGENCY NAME(S) AND ADDRESS(ES) U. S. Army Research Office P. O. Box 12211 Research Triangle Park, NC 27709-2211				10. SPONSORING/MONITORING AGENCY REPORT NUMBER ARO 32327.1-CH	
11. SUPPLEMENTARY NOTES The view, opinions and/or findings contained in this report are those of the author(s) and should not be construed as an official Department of the Army position, policy, or decision, unless so designated by other documentation.					
12a. DISTRIBUTION/AVAILABILITY STATEMENT Approved for public release; distribution unlimited.				12b. DISTRIBUTION CODE	
13. ABSTRACT (Maximum 200 words) We report on continued work to develop and demonstrate the use of infrared fiber optics to probe the decomposition processes in burning gun propellant strands. Our experiments involve measuring the absorption across an open gap between two embedded fibers as it fills with gaseous decomposition products. Several improvements have been made to the experimental technique. In the most significant, detection techniques for the nitrogen oxide species NO ₂ and NO have been added to the N ₂ O detection system developed in earlier work. NO ₂ detection was accomplished by differential absorption of red and green HeNe lasers, while NO detection used a tunable infrared diode laser. We have observed N ₂ O, NO ₂ and NO evolving into the observation volume during the burning of an RDX-based composite propellant. Observations to date indicate that NO appears at similar times as N ₂ O, that is, while the observation region is relatively cool and far from the burning surface, while NO ₂ can significantly precede both NO and N ₂ O. These data will provide additional information on the physical and chemical processes in the condensed phases of this composite propellant.					
14. SUBJECT TERMS solid propellant combustion infrared fiber optic absorption diagnostic				15. NUMBER OF PAGES 34	
				16. PRICE CODE	
17. SECURITY CLASSIFICATION OF REPORT UNCLASSIFIED	18. SECURITY CLASSIFICATION OF THIS PAGE UNCLASSIFIED	19. SECURITY CLASSIFICATION OF ABSTRACT UNCLASSIFIED	20. LIMITATION OF ABSTRACT UL		

**EMBEDDED INFRARED FIBER OPTIC
ABSORPTION STUDIES OF
NITRAMINE PROPELLANT
STRAND BURNING**

Final Report

Prepared by

J. Wormhoudt, P. L. Kebabian, and C. E. Kolb
Center for Chemical and Environmental Physics
Aerodyne Research, Inc., 45 Manning Road, Billerica, MA 01821

Prepared for
U. S. Army Research Office
Under Contract DAAH04-93-C-0053

October 1994

APPROVED FOR PUBLIC RELEASE;
DISTRIBUTION UNLIMITED

DTIC QUALITY INSPECTED 1

TABLE OF CONTENTS

1.0	INTRODUCTION	1
2.0	EXPERIMENTAL TECHNIQUES	3
2.1	NO ₂ Detection Technique	3
2.2	NO Detection Technique	6
2.3	Fiber Preparation and Insertion	9
3.0	EXPERIMENTAL ANALYSIS	12
4.0	EXPERIMENTAL RESULTS	14
5.0	DISCUSSION	22
5.1	Review of Measured Parameters	22
5.2	Relation of Observations to Chemical Mechanisms of Decomposition	25
6.0	SUMMARY	29
7.0	REFERENCES	30
8.0	LIST OF PUBLICATIONS AND TECHNICAL REPORTS	32
9.0	LIST OF PARTICIPATING SCIENTIFIC PERSONNEL	33
10.0	REPORT OF INVENTIONS	34

Accession For	
NTIS GRA&I	<input checked="" type="checkbox"/>
DTIC TAB	<input type="checkbox"/>
Unannounced	<input type="checkbox"/>
Justification	
By _____	
Distribution _____	
Availability Codes	
Dist	Avail and/or Special
A-1	

LIST OF FIGURES

Figure 1.	High Pressure Strand Burner, Propellant Strand, and Embedded Fiber Optics	4
Figure 2.	Schematic Drawing of Infrared Fiber Optic Absorption Experiment	5
Figure 3.	Optical Layout of Tunable Infrared Diode Laser Spectrometer Table	7
Figure 4.	Original Fiber Insertion Procedure	9
Figure 5.	Predicted Transmission Spectrum for 0.2 Mole Fraction NO at 6 atm and 300 K Over a 0.3 cm Path	13
Figure 6.	Observation of N ₂ O Using Drilled Holes in XM39 Strand, at 6 atm Pressure	14
Figure 7.	Simultaneous Observation of NO ₂ in XM39 Strand (6 atm Pressure)	16
Figure 8.	Simultaneous Observation of N ₂ O and NO ₂ . Experiment using drilled holes in XM39 strand, at 6 atm pressure, with 60 Hz data averaging.	17
Figure 9.	NO Region Tunable Diode Laser Transmission Spectra Near Loss of Transmission Point	18
Figure 10.	NO Region Tunable Diode Laser Transmission Spectra Immediately Following Spectra in Figure 9	18
Figure 11.	Time History for NO/NO ₂ Experiment- NO and NO ₂ Data Shown at 10 Hz, Temperature at 30 Hz, Fiber to Burning Surface Curve Fit Through 1 Hz Data	19
Figure 12.	Thermal Wave for NO/NO ₂ Observation of Figure 11	21
Figure 13.	Qualitative Sketch of Typical Thermal Waves and Positions of Other Events in Strand Burning Observations	24
Figure 14.	Major RDX Decomposition Gas Species Mole Fractions from Experiments of Fetherolf and Litzinger ⁷⁻⁸ Compared to Adaptation of Observations of Behrens ⁶ (dots)	27

LIST OF TABLES

Table 1. Composition of XM39 Propellant	1
Table 2. Averages and Ranges of Quantities Measured in XM39 N ₂ O Experiments	23

1.0 INTRODUCTION

This is the final report for Contract DAAH04-93-C-0053 from the U. S. Army Research Office. This one-year program continued work begun under Contract DAAL03-91-C-0008. The work performed under both programs was a response to the need for the development of new diagnostic techniques to monitor the progress of decomposition and ignition kinetics in the condensed phase. We investigated the use of embedded optical fibers, using infrared-transmitting fibers in a direct absorption experiment, in which a gap between a pair of embedded fibers allowed spectroscopic detection of decomposition products within a strand of solid propellant.¹⁻³ We found that detection of these species coupled with other simultaneous measurements can provide a wealth of information about the region which produces the decomposition gases, even though it lies substantially closer to the burning surface than does our observation region.

A series of observations of the appearance of the known nitramine decomposition product N_2O led us to suggest the existence of a layer of the burning composite propellant strand which was neither completely solid nor completely liquid. Such a region could exist because of the lower decomposition temperature of RDX (the major component of the XM39 composite propellant we studied— see Table 1) compared to that of the plastic binder.

Table 1. Composition of XM39 Propellant

Component Name	Chemical Formula	Mass Fraction	Melting Point
RDX (5 micron)	$C_3H_6N_6O_6$	0.76	190°C
Cellulose Acetate Butyrate (CAB)	$C_{15}H_{22}O_8$	0.12	215-225°C
Nitrocellulose (NC)	$C_6H_{7.55}O_5(NO_2)_{2.45}$	0.04	160-170°C
Acetyl Triethyl Citrate (ATC)	$C_{14}H_{22}O_8$	0.076	(B. P. 132°C)
Ethyl Centralite (EC)	$C_{17}H_{20}ON_2$	0.004	72°C

Our evidence for this region lies in the fact that our observation volume is at a temperature well below the RDX melting point when N_2O is forced into it from a region nearer the flame front. We know that it is at a low temperature not only from thermocouples embedded in the observation plane, but also simply from the fact that transmission through the observation volume is often maintained for a second or more after the first appearance of N_2O . This would not be possible if liquid RDX were near enough to the walls of the observation volume to cut off transmission. Yet we know from previous experimental work^{4,5} that decomposition of RDX into gaseous products only proceeds at an appreciable rate after it liquefies. Still, the RDX which produces the decomposition gases we see cannot be in the totally liquid layer observed at the gas/condensed phase interface, since bubbles formed in the liquid layer would be much more likely to burst upward into the gas phase rather than to inject gas downward into our observation volume within the solid. Only if some bubbles were trapped within a matrix formed by the propellant binder would we see abrupt appearance of large mole fractions of gaseous decomposition products, consistent with pressurized bubbles releasing gas into suddenly opening cracks in the propellant.

The overall goal of the work reported here was to confirm that our observations are indeed of the gaseous products of condensed phase decomposition of RDX in a burning composite propellant. Mass spectrometric observations of RDX decomposition by several investigators, in particular the thermal decomposition/molecular beam mass spectrometry work of Behrens⁶ and the laser-supported strand burning/microprobe mass spectrometry observations of Litzinger and co-workers⁷⁻⁸ have shown that about half a dozen major species are evolved. The observation of the simple presence or absence of several of the more reactive species could serve to distinguish between products of condensed-phase decomposition and primary combustion.

As the species to address in the present work, we chose NO and NO_2 . As will be explained in the discussion section, these two species together with N_2O serve to outline the three global steps in the most widely accepted mechanism of RDX decomposition. In addition, they each require a modification of our experimental technique from the use of a pair of infrared bandpass filters as in our earlier work. Because these new detection techniques both involved lasers, it was in fact more practical to set up simultaneous detection of two species than if the filter technique had been used in three or more bands. Both NO and NO_2 were detected, confirming that we are observing decomposition gas. We will describe and discuss these observations, after a description of the new detection techniques and several other significant apparatus upgrades.

2 0. EXPERIMENTAL TECHNIQUES

The basic experimental concept, burning of propellant strands with embedded optical fibers as well as conventional diagnostics, remains unchanged and is illustrated in the strand burner drawing in Figure 1. However, the light sources and detectors at the input and output fibers have changed as we have targeted additional chemical species, and our methods of preparing and inserting fibers have also evolved.

The only propellant studied to date has been XM39, composed of 76% RDX and 24% binder. Experiments have been performed at 2 pressures, 1 and 6 atm, although the new observations reported here were all 6 atm experiments. We use secondary combustion of the gaseous decomposition products with air to support the primary combustion of the solid propellant. A combination of nitrogen addition to the air and a large enough flow velocity around the strand is used to prevent burning down the side of the strand. At 6 atm, the air and N_2 flows are 2470 and 825 STP cm^3/s , respectively, so the velocity of the gas flow around the strand is around 7 cm/s. Under these gas flow conditions, the strand burns with a roughly flat melt layer. In our previous work, we measured propellant burning rates of about 0.015 cm/s at 1 atm, and 0.041 cm/s at 6 atm. A high-resolution video system is used to record each burn. The beginning of data collection is accompanied by a computer signal to the video recorder which starts its time clock.

2.1 NO₂ Detection Technique

A schematic diagram of the experiment configured for simultaneous detection of N_2O and NO_2 is illustrated in Figure 2. The tuning fork chopper with mirrored blades modulates the light from an infrared source (a globar) and two visible lasers at approximately 1200 Hz. The propellant strand is mounted inside a high pressure strand burner. The embedded fluoride glass optical fibers (nominal diameter 200 μm) are connected to input and output fibers at the baseplate of the strand burner. Also passing through the baseplate are thermocouple leads and leads connecting a variac and a V-shaped segment of nichrome ribbon pressed against the top of the strand to provide ignition. The gaps between the source and detector fibers are in the 0.2 to 0.5 cm range. Infrared light collected by the fiber on the detector side is divided by a 50/50 beamsplitter and passes through a pair of narrow band infrared interference filters before being focused onto InSb infrared detectors. The visible light from the two lasers is reflected from the back of the infrared lens

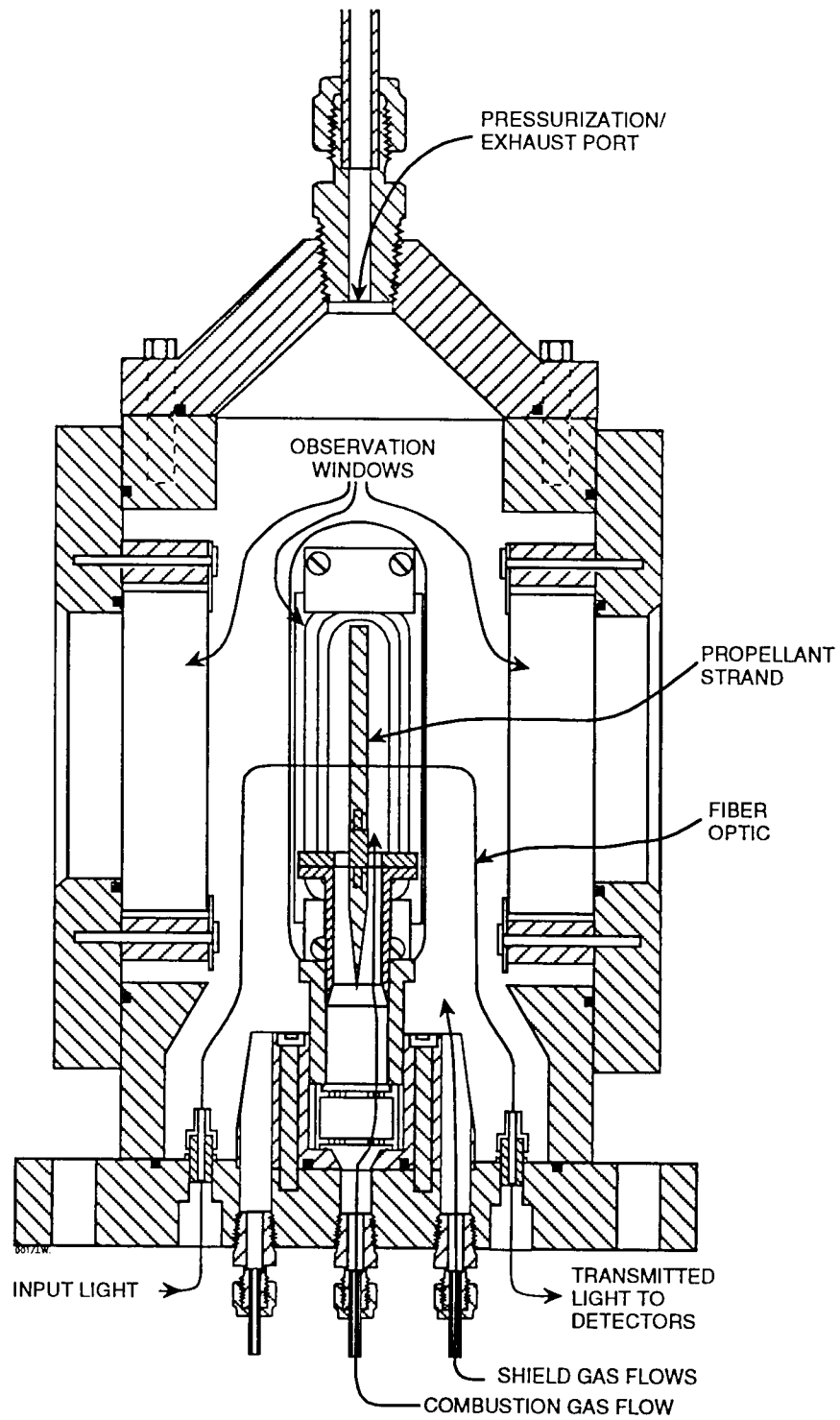


Figure 1. High Pressure Strand Burner, Propellant Strand, and Embedded Fiber Optics. The strand burner is a copy of a device in use at the U.S. Army Research Laboratory, Aberdeen Proving Ground, with some modifications to accommodate fiber optics.

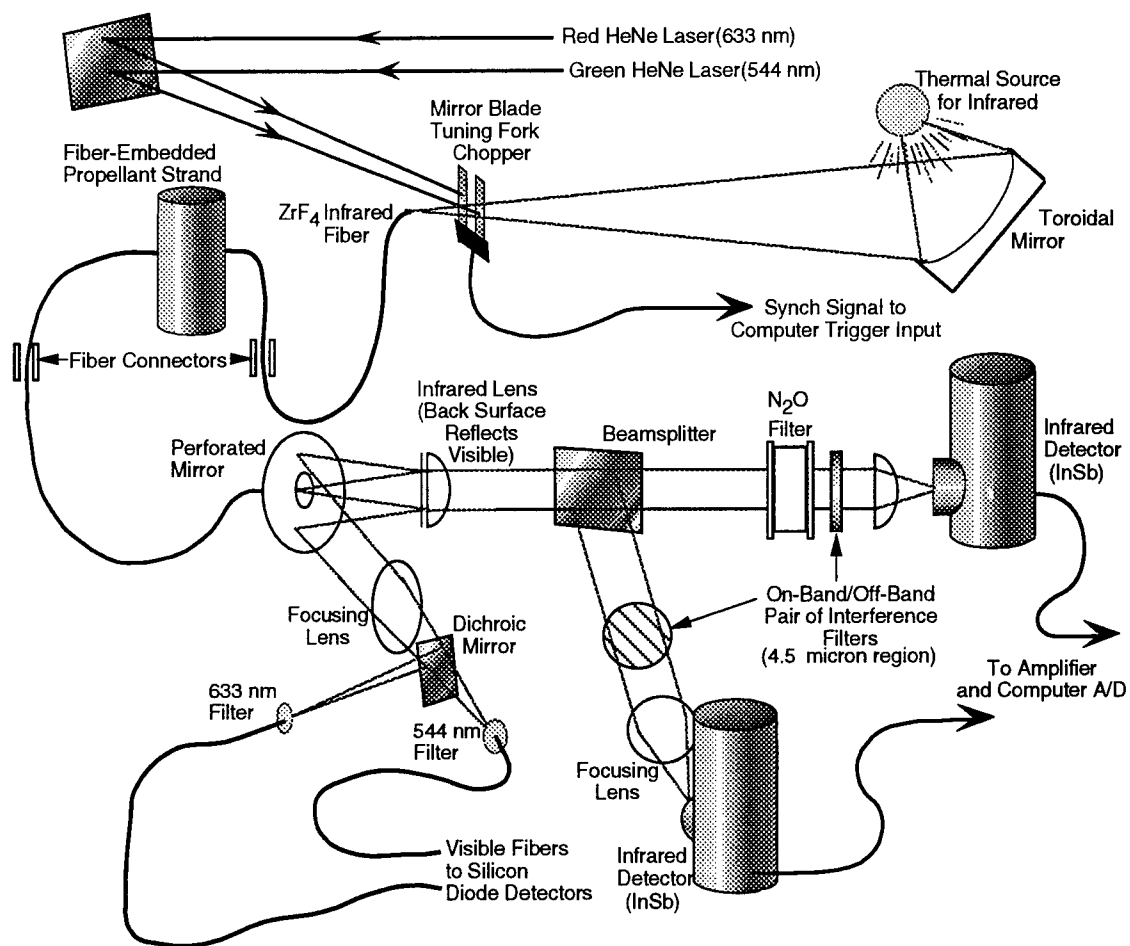


Figure 2. Schematic Drawing of Infrared Fiber Optic Absorption Experiment. In this configuration, N₂O is detected using pairs of infrared bandpass filters and infrared detectors, and NO₂ by the differential absorption of red and green HeNe lasers.

downstream of the output fiber, then collected by a perforated mirror and focused by a lens onto two visible-transmitting fibers which deliver the light to silicon phototransistors. A dichroic mirror serves to separate the red and green beams, with bandpass filters providing additional separation and room light rejection.

A data acquisition computer reads a signal point from each infrared and visible detector at each on and off point of the chopper. Readings from two embedded thermocouples are obtained at a slower (30 Hz) rate. Computer data acquisition for each chopper cycle is triggered by the synchronization signal from the chopper controller. The signals from the infrared detectors and pre-amplifiers and from the visible phototransistors pass through buffer amplifiers to minimize the effects of the analog to digital conversion. This also allows optimization of the time response of the signal, so the single data point the computer reads is representative of the entire half-cycle of the chopper.

2.2 NO Detection Technique

Several experiments were conducted using the $\text{N}_2\text{O}/\text{NO}_2$ setup, after which the apparatus was modified to allow simultaneous detection of NO_2 and NO , and a single such experiment was carried out. NO detection was achieved using a tunable lead salt diode laser, which is part of a laser spectrometer constructed for NASA to measure NO and other species in jet engine exhausts, combustors, and combustor simulators.

The tunable diode laser source we used is part of the combined *in situ*/extractive sampling system shown in Figure 3. The laser diode is housed in a dewar that allows precise control of the temperature, since this is the primary means of adjusting the laser output wavelength. The recent introduction of lead salt diodes that can operate in the 80-100 K range allows the use of liquid nitrogen cooled dewars. A laser control module provides current to the laser diode which is sufficient for lasing and which serves as a fine control on the laser wavelength. Rapidly scanning the laser current drives the output frequency across the spectral range of interest.

The wide-angle output from the laser is collected using a 15X reflecting microscope objective. The infrared beam is coaligned with a visible (HeNe) laser beam to facilitate alignment, using a dichroic beamsplitter. The fourth port of the dichroic beamsplitter can be used to observe

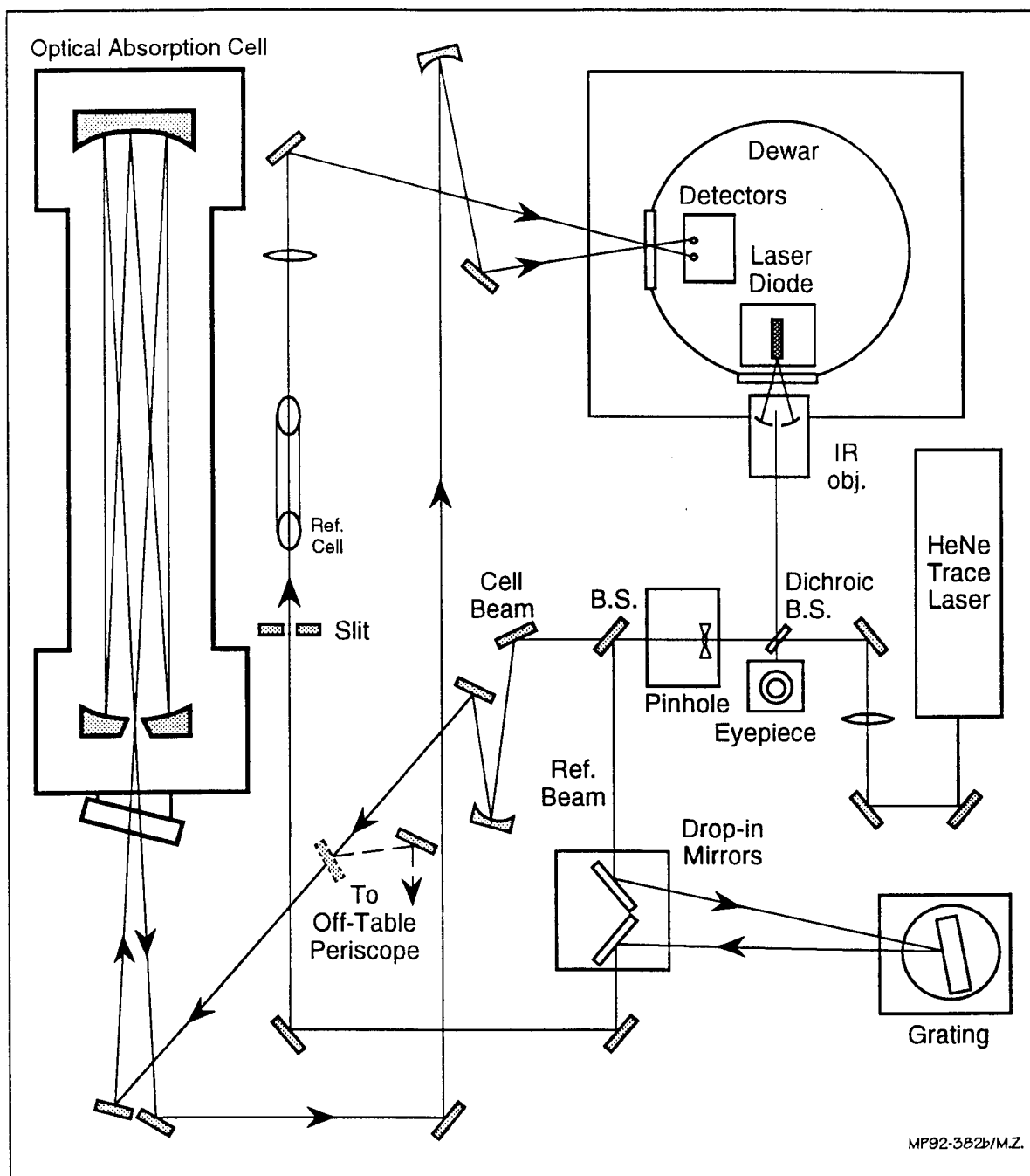


Figure 3. Optical Layout of Tunable Infrared Diode Laser Spectrometer Table.

the laser diode during alignment using an eyepiece which forms an effective 150X microscope. The IR microscope objective is adjusted using an XYZ translation stage until visible and infrared beams are verified to be coaligned by their transmission through the 200 μm pinhole (removed during instrument operation). A reference leg with a gas cell provides an absolute frequency scale from the known NO absorption line positions. A monochromator is included in the reference beam path to provide coarse-scale wavelength information and to determine if additional laser modes are present. The HeNe trace beam is used to accurately calibrate the monochromator, via higher order diffraction.

The diagnostic beam which passes through the infrared beamsplitter can be sent either to the long path absorption cell (not used in our experiment) or to a series of steering mirrors which send it off the laser table to a focusing lens on the strand burner table. The spherical mirror shown between the infrared beamsplitter and the off-table periscope mirrors in the diagnostic or cell beam path in Figure 3 results in a narrow, almost collimated beam (approximately $f/200$). On the strand burner table, the thermal source (globar) and its focusing mirror were removed, as was the mirrored tuning fork chopper. The red and green HeNe lasers were reflected into the input fiber using a tiny mirror placed at the same point as one blade of the tuning fork chopper. The diode laser beam passed through its focusing lens and past this scraper mirror directly onto the fiber. No mechanical modulation of this beam was used because the rapid spectral scanning of the laser serves the same purpose. The red and green HeNe lasers were modulated using a 400 Hz wheel chopper. At the output fiber end of the optical train, the diode laser was detected using one of the two InSb detectors which had been used for the thermal source. Since only one infrared detector was used, the infrared beamsplitter was removed, as was the bandpass filter (and the N_2O filter cell, since it happened to be the reference detector which was used). In addition, a filter capacitor which had been inserted in one stage of amplification of the infrared signal was removed to allow response to the much faster diode laser spectral sweeping rate.

The diode laser data acquisition method is based on rapid sweep integration. This is accomplished by scanning the laser frequency under computer control and synchronously measuring the transmitted infrared light intensity. The laser temperature and current are controlled by a Laser Photonics controller. The laser temperature is held constant while the current through the laser is modulated with a computer generated sawtooth to sweep the output frequency across the spectral interval. The sawtooth is generated in discrete steps (50, in our experiment) with a digital to analog converter board. The spectrum was scanned at a rate of 1.5 kHz. At the end of each scan the laser current is dropped below the lasing threshold to provide a precise measurement of zero light intensity. The detector output is read by a Scientific Solutions Lab Master AD data acquisition board and transferred to the extended memory of the diode laser controlling computer

using direct memory access (DMA). Spectra taken at the 1.5 kHz rate are averaged and written to a RAM drive at a 30 Hz rate.

2.3 Fiber Preparation and Insertion

In our previous work¹⁻³ the fibers were embedded in propellant strands by cutting the strands, pressing grooves in each face, positioning the fibers, and reattaching the two pieces of propellant using cyanoacrylate adhesive. This technique is shown in Figure 4. We often observed

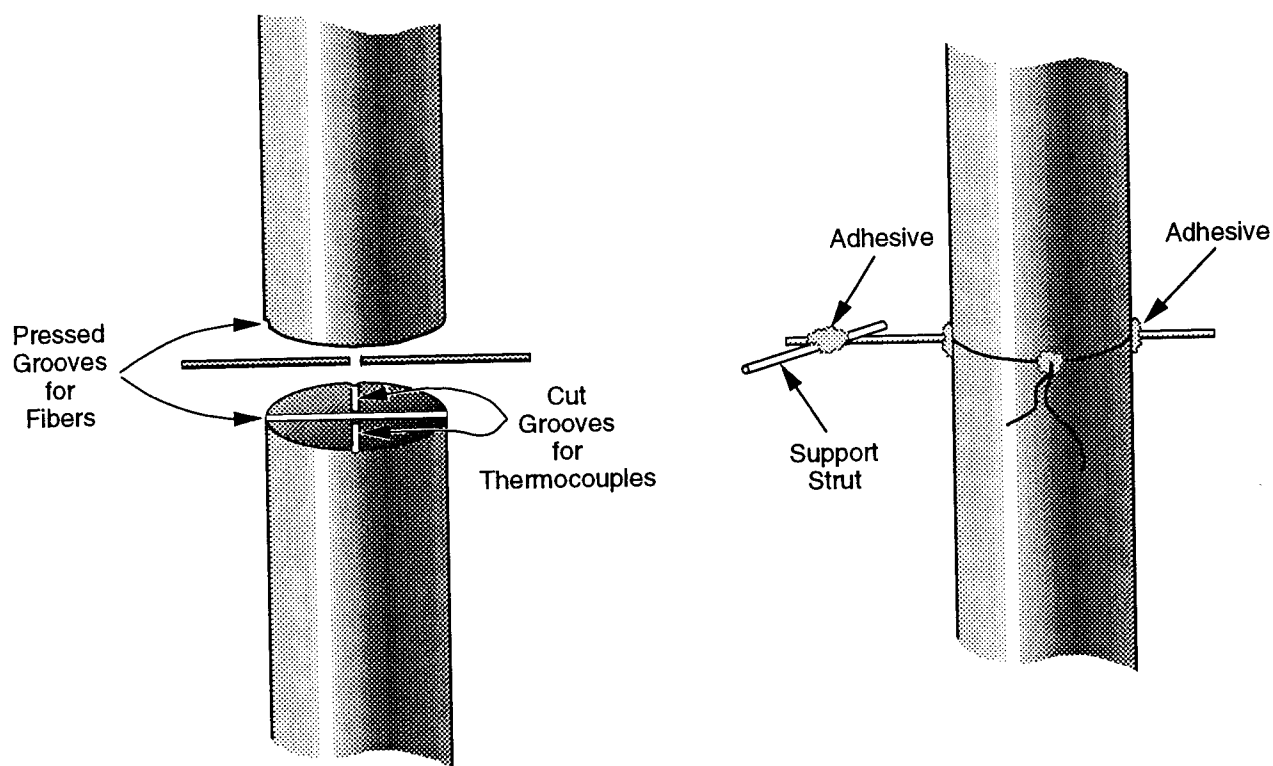


Figure 4. Original Fiber Insertion Procedure

burning rate perturbations as the flame front passed through the fiber insertion region, and we were concerned that the operation of pressing grooves into the propellant might be generating the cracks we believed were carrying decomposition gases from a region containing liquid RDX to our observation volume. Therefore, in our continuing work we invested some effort in developing the capability to drill holes through the strands which are snug fits for our fibers. In principle, this allowed fiber insertion without any of the intrusive features (saw-cut and adhesive) detailed above.

In practice, we found that while the old insertion technique had allowed us to observe transmission through the fibers for up to several seconds after decomposition gas appearance, the new technique resulted in much earlier losses of transmission. We believe this was because the adhesive applied to the outside of the strand had acted as enough of a heat sink that the center of the strand burned faster than the outside. With drilled holes, the burning surface was flat, not concave, and only a slight tilt would result in one fiber or the other burning through before any gas was observed in the center of the strand. The observations presented earlier in the present contract⁹ used drilled holes with no adhesive (and were obtained after a number of trials which yielded no observations at all). We then performed additional experiments in which small amounts of adhesive were applied to the outside of the strand at the fiber insertion plane (but not associated with the fiber insertion points). Observation times were indeed increased, and we concluded we could use this technique of properly shaping the burning surface without worrying that it was the source of our observations of N_2O and NO_2 . Observations presented here used this technique.

Several other modifications to the apparatus described in our previous final report² can be noted. First, a toroidal mirror replaced a lens for better collection of light from the thermal infrared source. Second, where the infrared fibers used to pass through the baseplate of the strand burner without interruption, now each segment (input and output) has been replaced by two lengths of fiber joined by SMA connectors at the baseplate. Only the short segment from the baseplate to the strand is now lost after a burn, while the longer segments, from the source to the burner and from the burner to the detection optics, remain intact. Finally, assembly problems led us to develop a technique of forming the fibers to adopt the shape shown in Figure 1.

The problem was that our initial technique of bringing the fiber from the baseplate to the propellant strand was to leave enough extra fiber that all bends were gradual. The advantages of this were that the fiber would not break during insertion, and that there would be little spring force which might misalign the fibers earlier in the burn as the propellant began to soften. The disadvantage was that so much slack in the fiber meant that the shell of the strand burner often broke the fiber as it was being lowered to complete the assembly. We reasoned that if fibers could take the actual shape shown in Figure 1, conforming to the shape of the strand burner shell, they

would be safe from such mishaps, and shorter lengths of fibers would be required. After some experimentation, we found that we could heat the fibers to a point where they would soften, then set upon cooling. A mandrel of the proper (0.75 inch) radius was equipped with an attached thermocouple and resistance heater driven by a temperature controller. For our standard 200 μm diameter fluoride glass fiber, a controller set point temperature of 230°C worked well. Making one 90° and two 45° bends resulted in a fiber segment which was easily inserted and in no danger of being broken upon final strand burner assembly. We even found the same technique could be applied to 300 μm fiber which would have otherwise have been too stiff to be usable. Without converting our entire system to this fiber, we could not realize significant gains in transmission, but in future work such a conversion should result in a signal gain of about a factor of two.

However, we have noticed one new phenomenon which, because its appearance coincides with the above fiber-bending technique, we will discuss here. In our last three experiments, visible transmission was seen to drop to zero while infrared transmission remained finite. In the first of those observations, using 300 μm fibers, post-test examination clearly showed that fine transverse cracks had appeared in both input and output fibers, near the entrance points to the strand. These cracks were narrow enough that they strongly affected the visible light, while passing the infrared light almost unattenuated. In the final two tests (whose results will be presented below), using 200 μm fibers, we cannot be certain that fiber cracking was involved - if cracks were formed, they were in a part of the fiber which was subsequently destroyed by the flame. We will see that there are other possibilities for the observed transmission histories in addition to artifacts induced by fiber preparation methods, but the possibility that our forming technique results in strained fibers which are predisposed to cracking cannot be ruled out until more tests are done.

3.0 EXPERIMENTAL ANALYSIS

As detailed previously,¹⁻³ N₂O detection involved infrared bandpass filters centered near 2210 cm⁻¹ (N₂O-sensitive region) and 2145 cm⁻¹ (reference band). The filter responses were calibrated computationally, using Fourier transform infrared spectrometer measurements of the bandpass filter transmission curves, and N₂O spectral absorbance values derived from the HITRAN absorption line database,¹⁰ because this most easily allowed us to take into account changes in the in-band absorption due to changes in line strengths and widths with temperature.

Similarly, although we have made confirming absorption measurements of our own, the absorption coefficients we used to interpret the observations using the green (543.5 nm) and red (632.8 nm) HeNe lasers were taken from the literature.^{11,12} Specifically, we used absorption coefficients of 3.2 atm⁻¹ cm⁻¹ for the green and 0.45 atm⁻¹ cm⁻¹ for the red. Although these values were taken from room-temperature spectra, we had no evidence of strong temperature dependence in those spectral regions, and did not attempt to estimate corrections. Of course, the absorption coefficient of NO₂ can depend on its temperature in another way, through the NO₂ - N₂O₄ equilibrium. Still, at 6 atm and 100°C, typical conditions if we continue to assume that the injected decomposition gases have cooled to the temperature of the observation region as indicated by the embedded thermocouples, the NO₂ fraction is still about 0.75, so dimerization will not affect the qualitative results reported here.

The transmitted intensity signals from the thermal infrared and visible laser detectors are obtained from computer files of the detector outputs by differencing each pair of chopper-open and chopper-closed values. These intensity records are then averaged— an average of 40 pairs of points yields a 30 Hz data record, and for noisier data 10 Hz or 5 Hz averages are used. After the fiber has burned through, the remaining data stream is averaged to give a zero level which is subtracted from each detector signal before the ratio is taken. The value of this ratio, relative to its value before ignition, gives a fractional transmission in the N₂O or NO₂ spectral region which is compared with the calibrations described above to yield column densities.

The analysis of the NO laser absorption data was directed towards the same quantity, a time history of fractional transmission at the peak of the NO absorption feature which can be converted to an NO column density. Once again, the HITRAN line compilation can be used to estimate what absorption would be observed for a given column density. Figure 5 shows such a calculation, for a path length of 0.3 cm, a pressure of 6 atm, an NO mole fraction of 0.2, and a temperature of 300 K. There are four strong NO absorption lines in this region, a closely spaced

doublet around 1896.99 cm^{-1} and two unresolvable lines centered at 1897.3537 cm^{-1} . Although the high pressure broadens all of these lines together, the asymmetry due to the high frequency pair is still observable. The spectral scale in Figure 5 corresponds roughly to the region scanned in our experiment. As noted above, the diode laser computer wrote 50-point files of laser intensity over the region at a 30 Hz rate. Averages of this intensity from early in the burn were used as reference curves (I_0) to convert later files to transmission spectra (I/I_0). It turned out that the NO time history could be seen most clearly if sets of three such spectra were averaged to give transmission measurements at a 10 Hz rate. We will see that a substantial (spectrally constant) loss of intensity precedes NO appearance, so that the spectra which show an effect of stronger absorption at higher frequencies due to NO are quite noisy. Nevertheless, an additional spectral averaging to produce transmitted intensities in the ranges $1896.9\text{--}1897.15\text{ cm}^{-1}$ (near the peak) and $1896.3\text{--}1896.6\text{ cm}^{-1}$ (as near the wing as our diode laser mode would allow us to get) gave a ratio (or NO peak transmission) with a fairly good signal-to-noise ratio.

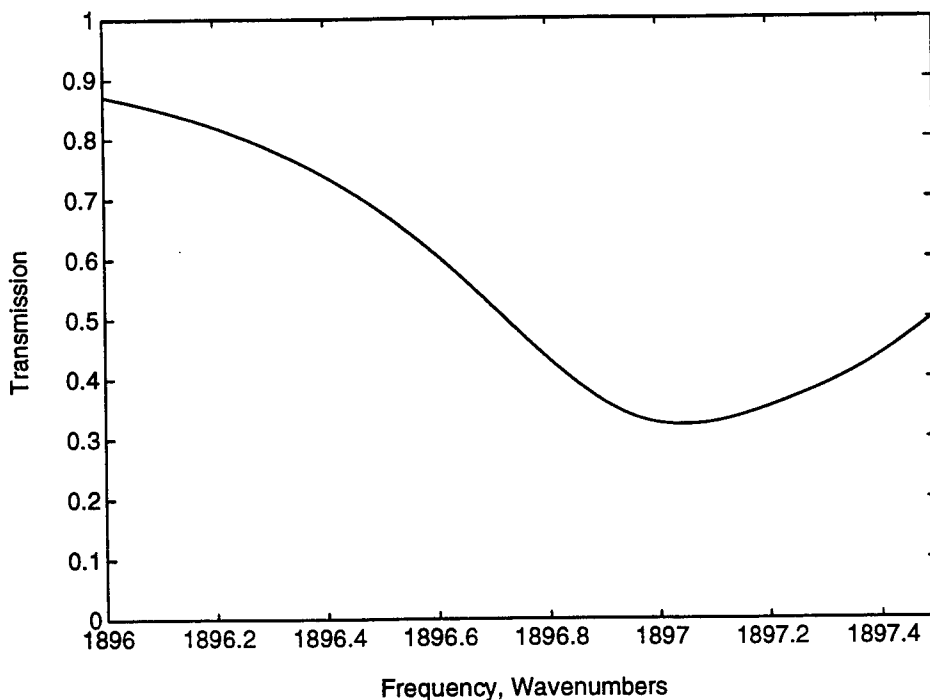


Figure 5. Predicted Transmission Spectrum for 0.2 Mole Fraction NO at 6 atm and 300 K Over a 0.3 cm Path.

4.0 EXPERIMENTAL RESULTS

We begin with an example of an experiment in which simultaneous observations of N_2O and NO_2 were made, for a strand in which fibers were inserted by drilling close-fitting holes, not by cutting and re-joining the strand around the fibers. We will first consider each species observation separately, then study the time relationship between the two. Figure 6 presents an example of the data traces near the time of N_2O appearance. The shorter time between N_2O appearance and transmission loss means that the observation is most clearly presented using intensities averaged to yield 60 Hz data streams. The figure shows the two detector intensities (both normalized to one at their maximum values), their ratio, and the embedded thermocouple temperature. The N_2O (as indicated by the drop in the ratio of detector intensities) appears and reaches a fairly constant level in less than 0.03 s, then maintains this level for about 0.03 s before continued loss of transmission causes the ratio to become meaningless. The abrupt appearance is consistent with the great majority of previous observations at this (6 atm) pressure.

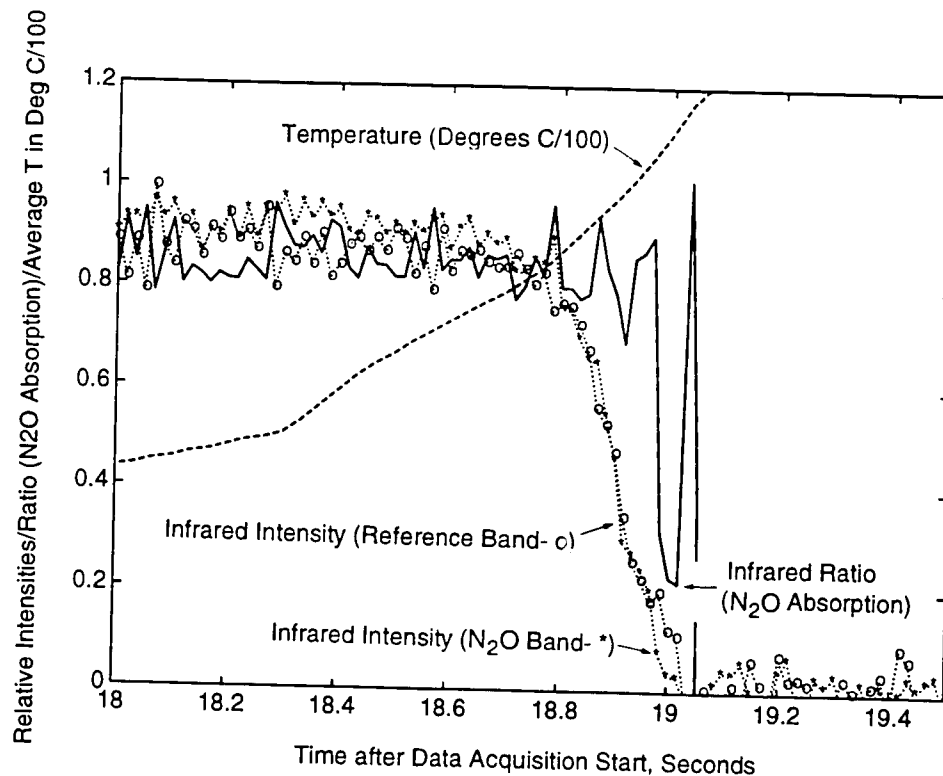


Figure 6. Observation of N_2O Using Drilled Holes in XM39 Strand, at 6 atm Pressure.

The time between N_2O appearance and transmission loss is much shorter than the 0.3 to 0.7 s range reported previously, for the reasons discussed above. In the earlier observations, averaging to yield 30 or even 10 Hz data streams was acceptable, while Figure 6 was obtained by averaging sets of only 20 points (60 Hz). Nevertheless, an examination of the original data shows that the averages properly represent what occurred: for all three 60 Hz data points showing substantial absorption by N_2O , the reference band intensity is above the noise level indicated at the right hand side of the figure, and at least one of the three N_2O band intensities can be considered to be above the noise level as well. If we assume that the N_2O is at the temperature of the embedded thermocouples (as discussed previously, an assumption with some uncertainty, but we have no better source of gas temperature information) we can use the known absorption path lengths to calculate an N_2O mole fraction of about 0.15 for this case.

The main point of this observation is that large N_2O mole fractions are still observed to appear abruptly in the observation region, even though no cutting, pressing, or gluing of the strand was involved. Furthermore, the temperature at which the N_2O appears (about 100°C) is consistent with the range of $35\text{--}155^\circ\text{C}$ previously reported¹⁻³. The distance to the flame front (from the video record) is about 0.085 cm, near the average of 0.15 cm observed previously.

In Figure 7 we present the observation of NO_2 using the visible detection technique taken simultaneously (and through the same fluoride glass fiber) with the infrared N_2O observation shown in Figure 6. The green/red intensity ratio, related to the peak transmission in the NO_2 band, has clearly begun to decline at about 18.8 s after data acquisition start. (That decline could have begun as early as 18.4 s, but there are two reasons to be uncertain about this: the short-term noise visible in Figure 7, and slower variations in the green/red ratio which twice in the preceding 18 seconds carry the ratio as low as that observed at 18.6 s. We attribute these slow variations to mode sweeping in the green HeNe laser. At no time do they carry the ratio below that at 18.6 s, so we are confident that the drop in peak transmission in the 18.8-18.9 s range is due to NO_2 and not to an experimental artifact.)

At the 18.8 s point the temperature has reached about 90°C , again well within the range at which we expect decomposition gas appearance based on our earlier observations of N_2O from XM39 burning at 6 atm. Even taking the change in transmission due to NO_2 appearance as lasting from 18.8 to 18.9 s, the derived NO_2 mole fraction for this case can be as large as 0.15. In other experiments, NO_2 mole fractions in the 0.05-0.06 range were observed. In our early observations,

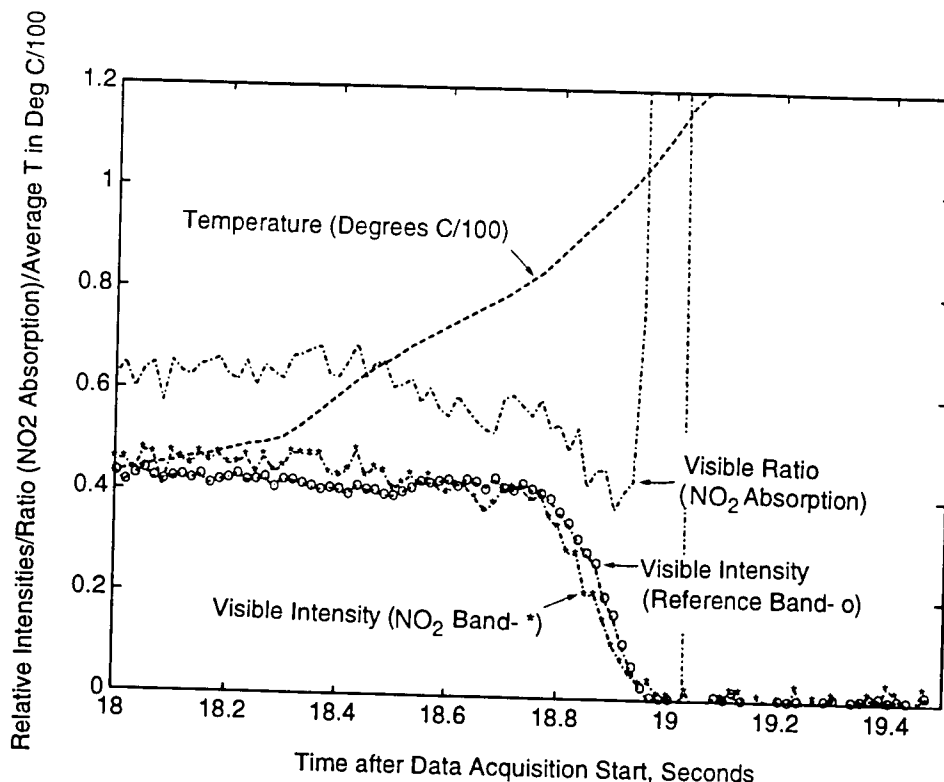


Figure 7. Simultaneous Observation of NO₂ in XM39 Strand (6 atm Pressure).

with very limited times before transmission loss, the appearances of N₂O and NO₂ seemed to be simultaneous. However, as seen in Figure 8 which puts the N₂O and NO₂ peak transmission histories in the same figure, NO₂ appears to precede N₂O by more than 0.2 s. This will be seen to be true of the NO₂/NO observation to be discussed next, although we will certainly need additional observations before we can be sure this is a general observation.

It can be seen in Figure 8 that the 60 Hz data point at which visible intensities in the (red) reference band drop to zero, driving the visible ratio to meaningless values, is one point before the first N₂O appearance point. In other words, all three infrared data points which show N₂O absorption occur after the visible transmission is zero in both channels. We mentioned above that one explanation for this is the appearance of cracks in the fiber which reflect and scatter visible light while still transmitting infrared, a phenomenon we were able to confirm in one set of fibers. Others possibilities exist which imply observations of interesting phenomena rather than of artifacts of the measurement technique. The most straightforward possibility might seem to be a large increase in the NO₂ mole fraction, since NO₂ does have a finite absorption coefficient at both visible wavelengths. However, this would require either an NO₂ mole fraction near 1 or a substantial error in our estimate of the NO₂ absorption coefficients, neither of which seems likely.

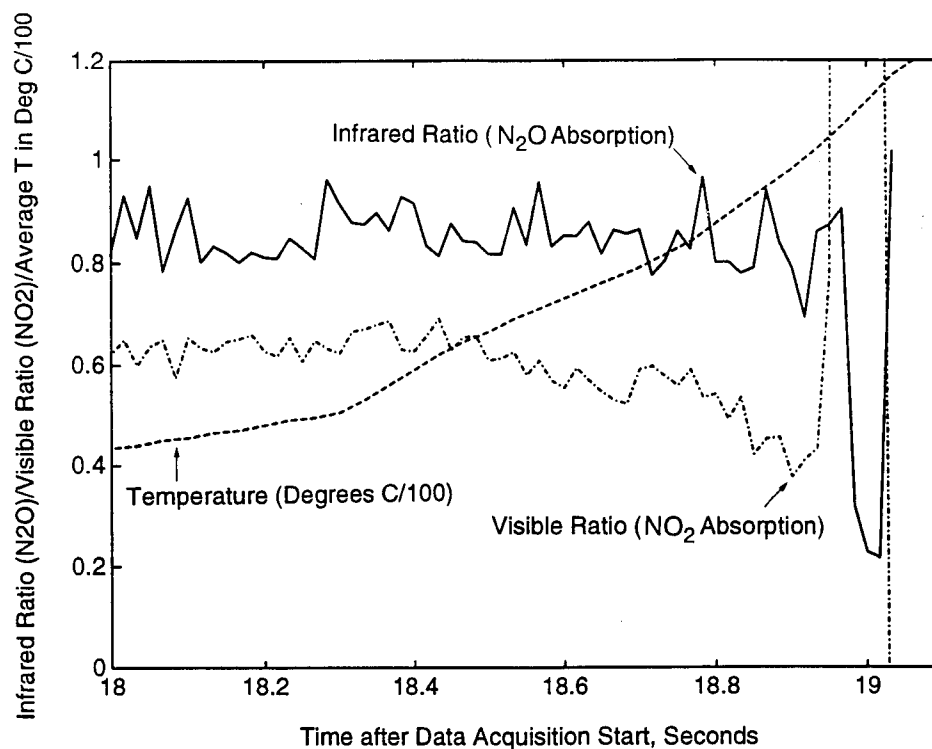


Figure 8. Simultaneous Observation of N_2O and NO_2 . Experiment using drilled holes in XM39 strand, at 6 atm pressure, with 60 Hz data averaging.

Another possibility might be smoke or other aerosol particles, which might be larger than the visible wavelengths but smaller than the infrared.

As our final example, we turn to our single experiment in which simultaneous observations of NO_2 and NO were made. As noted above, the thermal source had to be removed for this experiment so that no N_2O observations were made, but, from previous experiments, we have the most information on the correlation between N_2O concentration, temperature, and distance to the burning surface. Figures 9 and 10 show the last NO region spectra before loss of transmission, on the same scale as the model spectrum in Figure 5. Because the laser intensity is rapidly changing at each end of the scan, we can expect accurate transmission values only in the middle 30 or so points of the 50 point scan. In Figure 9, the four spectra are flat across this region, showing no systematic spectral variation. The first spectrum in Figure 10 (solid line) is flat as well, but the following three spectra clearly show lower values in the right hand region while showing appreciable transmitted light on the left, just as the model spectrum in Figure 5 would lead us to expect for a substantial NO absorption.

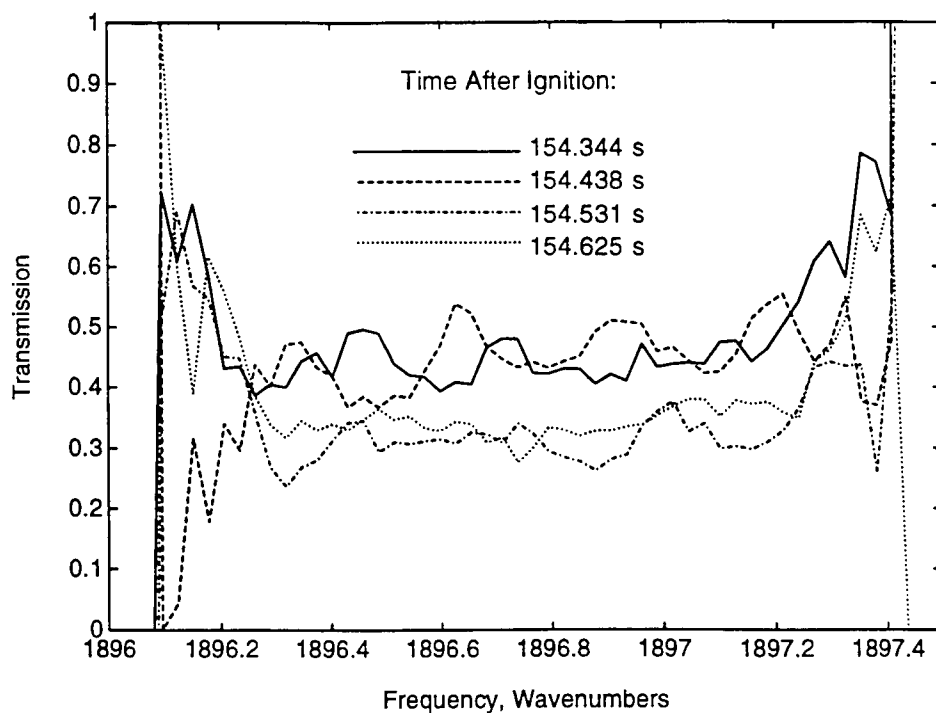


Figure 9. NO Region Tunable Diode Laser Transmission Spectra Near Loss of Transmission Point. Key gives time after ignition for the four spectra.

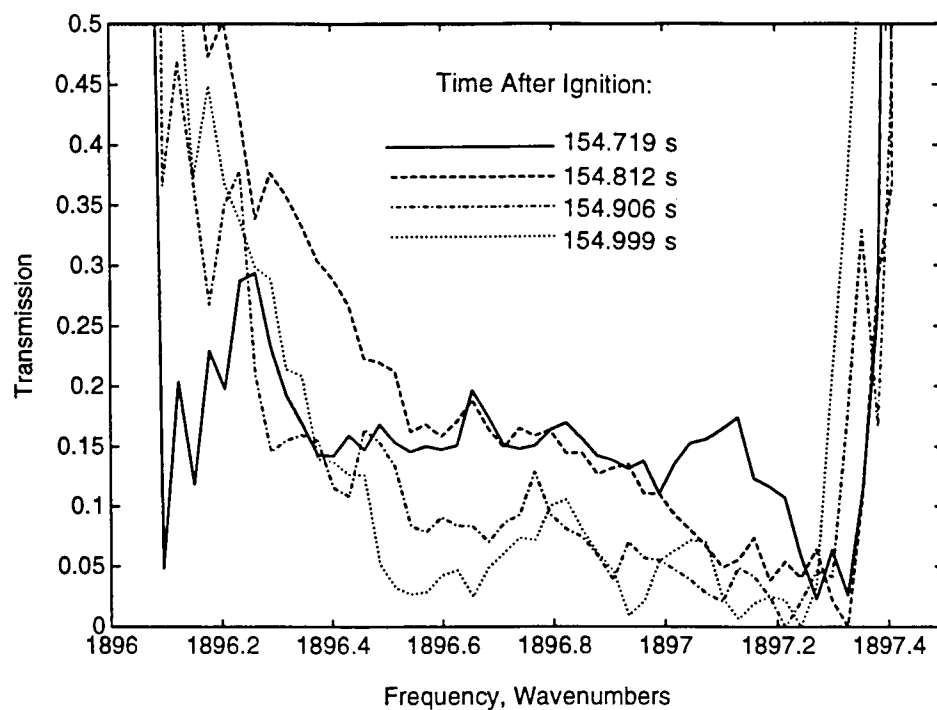


Figure 10. NO Region Tunable Diode Laser Transmission Spectra Immediately Following Spectra in Figure 9. Again, key gives time after ignition for the four spectra.

As described above, we integrated transmitted intensities in two bands, 1896.9 - 1897.15 cm^{-1} (peak) and 1896.3-1896.6 cm^{-1} (wing) to come up with a 10 Hz NO peak transmission time history. Those values are plotted in Figure 11, along with the green/red ratio which gives NO_2 concentrations, the embedded thermocouple temperature, and a distance to the burning surface transcribed from the videotape. Because the oscillations in NO_2 and NO ratios after transmission loss would obscure other data traces, we have truncated each ratio curve at the last meaningful point. Once again, it can be seen that the last meaningful visible ratio point coincides with the last infrared point before the appearance of a substantial mole fraction of decomposition gas.

We can deduce an NO mole fraction by comparing the NO peak transmission values in Figure 11 with the model calculation in Figure 5. We must realize that if the NO is warmer than

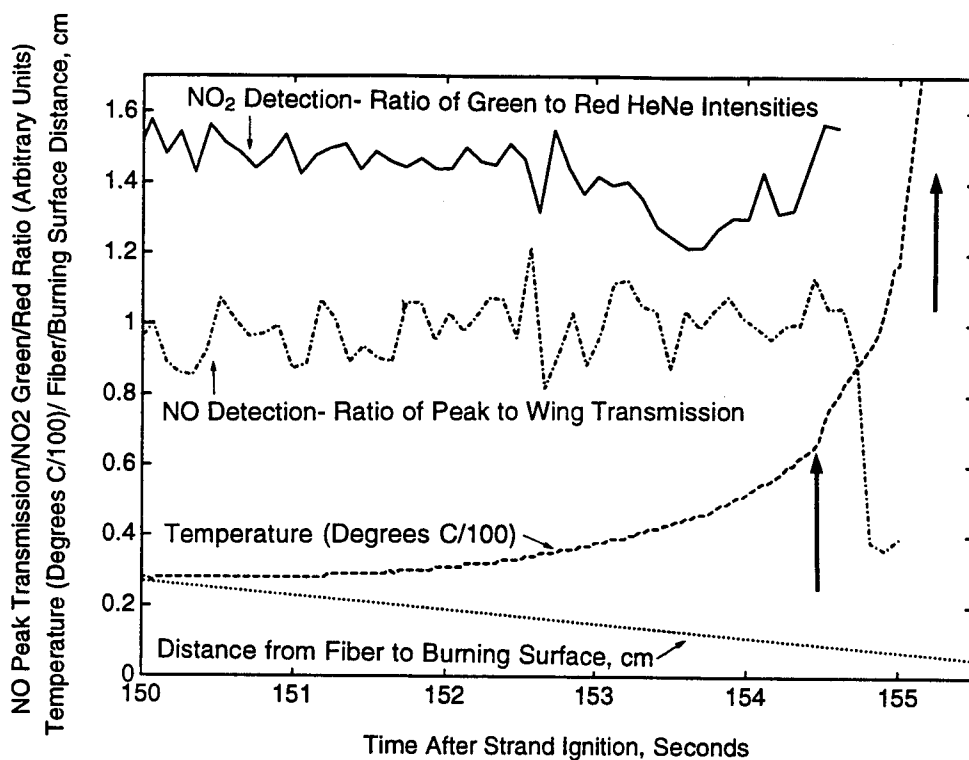


Figure 11. Time History for NO/NO₂ Experiment- NO and NO₂ Data Shown at 10 Hz, Temperature at 30 Hz, Fiber to Burning Surface Curve Fit Through 1 Hz Data. Arrows denote positions of the two transition points in the thermal wave (see text).

room temperature (the embedded thermocouple temperature at NO appearance is about 90°C) its absorption will be smaller for the same mole fraction because number density at a given pressure decreases with increasing temperature. Thus, while about a 0.2 NO mole fraction at 300 K would match the transmission in Figure 11, this would increase to a 0.26 mole fraction at 390 K. Clearly, the signal-to-noise ratio is such that there must be large error limits on these mole fractions, but we can at least be fairly certain that we have observed NO, at levels appropriate to RDX decomposition gases as measured by other workers. Furthermore, this NO observation has a time history very much like that observed repeatedly for N₂O: an abrupt appearance of a large mole fraction at about 0.1 cm from the burning surface. The NO₂ is once again seen to appear more slowly. Furthermore, it disappears, possibly due to reaction with the walls of the observation volume, before the NO appears.

Because the parameters measured in this last, NO/NO₂ run agree so well with the average values derived from the series of N₂O-only experiments in our earlier work, we will begin the discussion in the following section by reviewing those average values and the model for the physical characteristics of the burning strand which resulted from them. Of key importance to this model was the time history of the embedded thermocouple, which shows the thermal wave projected into the condensed phase propellant from the advancing burning surface. In Figure 12 we exhibit the same temperature trace as in Figure 11, but replotted on a semilog scale as a temperature difference from ambient. In this plot, the thermal wave into an inert propellant will be a straight line, since the temperature gradient is an exponential with a scale length related to the ratio of the thermal diffusivity of the propellant and its burning rate (see our earlier final report for a detailed discussion).² A change in slope with continued exponential behavior, such as at the point in Figure 12 marked "lower transition point", may be associated with a change in the physical properties of the propellant in the absence of an ongoing chemical change, such as a change in the thermal conductivity due to the appearance of cracks or voids in the solid. A deviation from exponential behavior, on the other hand, such as the one marked "upper transition point", denotes a chemical, heat-releasing or heat-consuming step. If the result is that the temperature gradient is shallower (extends further into the condensed phase), as we see above the upper transition point in Figure 12, this indicates heat release. In simple propellants this point indicated the position of the flame front, but in this composite propellant we believe it to be associated with the onset of RDX decomposition. The temperature at the upper transition point marked in Figure 12 is 198°C, while we expect burning surface temperatures to be more around 400°C. That temperature is reached at the point where the temperature gradient flattens out, consistent with passage of the thermocouple into the gas phase. The fact that this occurs at about -.029 cm by the video record indicates the

level of uncertainty of burning surface position measurement due to the slightly cupped surface. In this case only the edge of the strand could be seen in the video image.

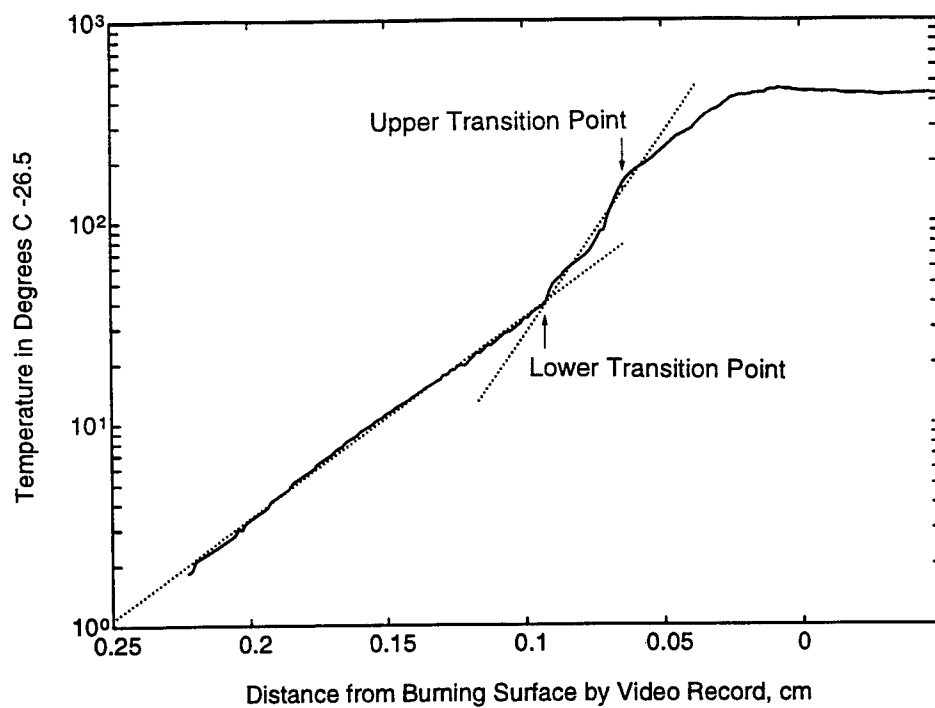


Figure 12. Thermal Wave for NO/NO₂ Observation of Figure 11.

5.0 DISCUSSION

5.1 Review of Measured Parameters

As a way of reviewing the parameters measured in our strand burning experiments and the evidence they provide for a model of the burning propellant, we compare the measured quantities in our last, NO/NO₂ measurement burn with Table 2 showing these quantities based on our N₂O-only work.³ The measured burning rate for our last run, 0.0396 cm/s, is within the standard deviation of the average for 6 atm cases. The NO mole fraction, like the range of N₂O mole fractions, is appropriate to pure RDX decomposition gas as characterized by other workers.⁶⁻⁸ The distances from fiber to burning surface at NO appearance are 0.094 and 0.078 cm for the actual video data record and the linear fit which suppresses disturbances at the fiber insertion plane. These values (and therefore the temperature at NO appearance of 94°C) are not significantly different from those in the table for N₂O. The filling of the observation volume with NO was essentially complete in one 60 Hz time increment, consistent with several observations of N₂O fill times equal to the time resolution used. A constant NO concentration is seen for three time steps or about 0.05 seconds, shorter than the 0.3-0.7 s range we saw using the cut-and-glue fiber insertion technique.

The time between NO appearance and the arrival of the burning surface (in the video record) at the fiber plane is 2.0 s, in the range of variation given in Table 2. Skipping down to the related entries at the bottom of the table, subtracting 0.089 cm (2.0 s times 0.0396 cm/s) from the video position at NO appearance of 0.094 cm gives a difference of 0.005 cm between these extrapolated and observed burning surface positions. The temperature at this point is 470°C, again in the range of variation shown in Table 2.

The distances to the burning surface of the two temperature history transition points marked in Figure 12 are about 0.095 and 0.065 cm. While we expect these values to remain roughly constant for the same propellant and pressure, we have argued that the more fundamental parameter in determining these changes in functional form is the temperature. The temperatures at the two transition points in the NO/NO₂ run are 72 and 198°C. Consulting Table 1, we can see that the upper transition point temperature is always near the melting point of RDX, which is in the 190-200°C range depending on purity. Since RDX, the major component of XM39, cannot decompose at significant rates until it melts, this correlation seems very likely. We have previously

Table 2. Averages and Ranges of Quantities Measured in XM39 N₂O Experiments

	<u>1 atm (7 cases)</u>	<u>6 atm (6 cases)</u>
Burning Rate, cm/s	0.0150±0.0014	0.0410±0.0025
<u>N₂O Appearance</u>		
N ₂ O Mole Fraction, Range	(0.05-0.19)	(0.05-0.24)
Flame-to-Fiber Distance at N ₂ O Appearance Point, cm		
From Point-by-Point Measurements	0.21±0.11	0.16±0.12
From Linear Fit to Flame Front Position	0.26±0.11	0.15±0.11
Thermocouple Readings at N ₂ O Appearance, Range, °C	(240-410)	(35-155)
Fill Time (from First N ₂ O to Steady Value), Range, s	(0.3-2.0) [5]	(0.1-0.3) [5]
(Numbers of Observations in Brackets)	(0.1-0.2) [2]	(0.7) [1]
Steady State Time (for Short Fill Time Cases, Time During Which a Roughly Constant Transmission Indicating N ₂ O Presence is Maintained), Range, s	(1-2)	(0.3-0.7)
Δt_{ff} , (Flame-to-Fiber Distance)/(Burning Rate), s	(8-28)	(1.7-4.8)
<u>Temperature History Lower Transition Point</u>		
Distance to Flame Front at Lower Transition Point, cm	0.34±0.17	0.07±0.07
Temperature at Lower Transition Point, T _l , °C	140±30	110±40
<u>Temperature History Upper Transition Point</u>		
Distance to Flame Front at Upper Transition Point, cm	0.26±0.085	0.05±0.06
Temperature at Upper Transition Point, T _u , °C	200±20	185±45
<u>Transmission Loss Point</u>		
Flame-to-Fiber Distance at Transmission Loss, cm	0.19±0.07	0.08±0.08
Temperature at Transmission Loss Point, °C	(250-500)	(50-330)
<u>Expected Time of Arrival of Flame Front at Fiber Plane</u>		
Distance to Flame Front at Δt_{ff} after N ₂ O Appears, cm	0.06±0.03	-0.02±0.06
Temperatures at Δt_{ff} after N ₂ O Appearance, °C	380±45	410±90

argued that the lower transition point, with a total range of observed values from 70 to 170°C, is related to a physical or chemical change related to the binder (acetyl triethyl citrate). Although a liquid in its pure state, it will have dissolved some of the other propellant components, so it is difficult to predict a temperature at which it or its decomposition products might be evolved except to say that it could very well be substantially lower than 200°C. Finally, the infrared transmission loss point for the NO/NO₂ run came at a distance to the burning surface of 0.0635 cm and a temperature of 187°C. As we have commented before, the large ranges of variation in the table indicate that transmission loss has not been consistently correlated with any one process, and so has neither a characteristic temperature or characteristic distance.

The thermal wave and fiber absorption parameters in Table 2 have been used as the basis of the cartoon in Figure 13, which gives approximations to the temperature histories observed at 1 and 6 atm. This figure reinforces the contention that the temperature history transition points are correlated with specific temperature ranges, independent of pressure and hence burn rate and distance from flame front. We have also contended that N₂O appearance, on the contrary, is not correlated with the temperature of the observation region, but rather with a distance from the

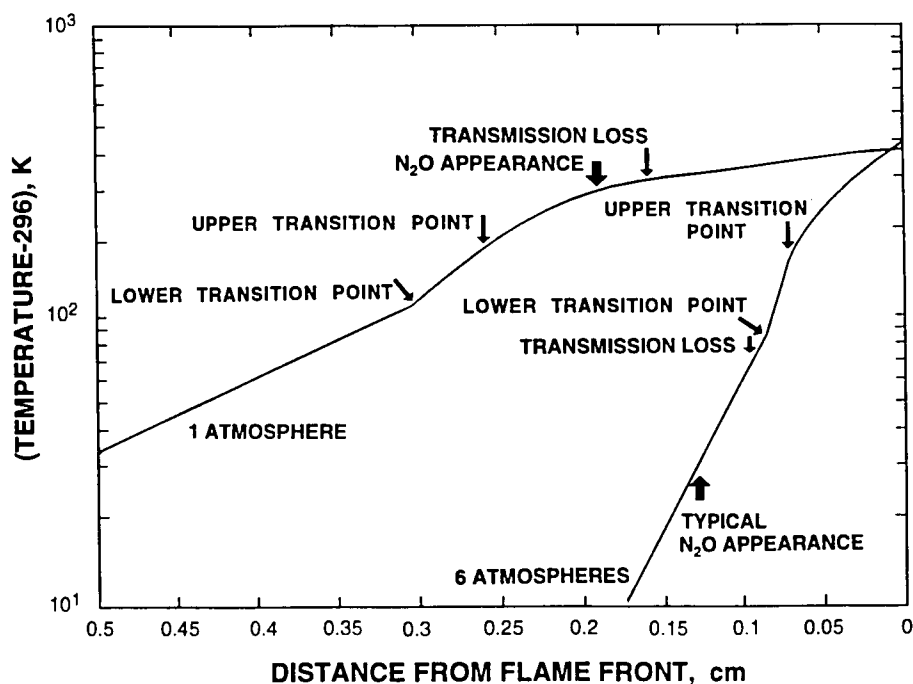


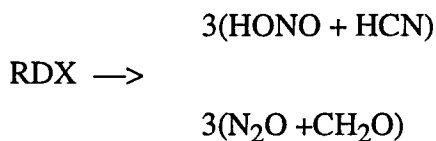
Figure 13. Qualitative Sketch of Typical Thermal Waves and Positions of Other Events in Strand Burning Observations.

burning surface and the high temperature condensed phase decomposition regions associated with it. Once the observation region is within this critical distance, cracks can open up which allow decomposition gas to fill it in the abrupt manner we have seen for N_2O and NO .

Slow filling, seen for N_2O at one atmosphere pressure, seems to be the rule for NO_2 even at 6 atm. We interpret this to mean that NO_2 is formed in a region nearer to the observation volume than the region which delivers pressurized decomposition gases in an abrupt filling event. These nearer regions would already be connected to the observation volume through existing cracks and connected voids in the composite propellant, so their production regions could not be as highly pressurized. Gas might simply effuse into the observation region as it was formed. This could be expected for N_2O at 1 atm because, as seen in Figure 13, under these low burning rate conditions the thermal wave reaches further into the propellant, and regions in which RDX can melt will be closer to the observation volume. For NO_2 , we can suggest that its slower filling rate may send the same message as the observation that it can substantially precede the appearance of either N_2O or NO : in strand burning, it is formed in cooler regions, before substantial amounts of the other two gases are produced.

5.2 Relation of Observations to Chemical Mechanisms of Decomposition

From the time we first began planning our experiments, we had as a goal the making of time-correlated measurements of enough species so that the relative amounts of the gaseous decomposition products could shed light on the competition between decomposition pathways. Brill¹³ has commented that the FTIR/fast thermolysis observations made by his group are consistent with the mass spectrometric studies cited above in that all support the existence of two global decomposition branches for bulk RDX, as put forward by Melius.¹⁴



It is generally assumed that the first microscopic step in the upper global branch is NO_2 production from N-NO_2 bond cleavage, so that NO_2 can be produced directly rather than by HONO decomposition. The first global branch is endothermic, the second exothermic, so it is expected that in experiments which do not resolve the kinetics of individual microscopic steps, N_2O production will be favored at lower temperatures, while NO_2 (rapidly produced from the reactive HONO) should be enhanced as the temperature increases. Brill's observations confirm this, but for RDX the effect is moderate, with $\text{N}_2\text{O}/\text{NO}_2$ ratio varying from 2.0 at 260°C to 0.8 at

almost 380°C. However, it is important to remember that these observations will only hold in kinetic regimes in which all the microscopic reactions contributing to each global branch are fast enough. Indeed, at high heating rates, N₂O production can be completely absent.¹⁸⁻²⁰

However, the observations of the Brill, Behrens, and Litzinger groups all show that at temperatures and heating rates expected in our strand burning from the region of RDX melting to the burning surface, the two global branches have competitive rates. Thus the seemingly different time behavior of NO₂ and N₂O in our experiments might come as a surprise. However, the Behrens and Litzinger experiments monitor systems which are closer to steady-state than to transient conditions, while the T-jump experiments of the Brill group, which begin with a high heating rate, do not monitor gaseous species until temperature equilibration is attained. Thus, a first suggestion for a reason why only our experiments show a kinetic difference between NO₂ evolution and that of other gases may lie in a combination of differences in steady-state or transient character and differences in time resolution.

Another difference which can be suggested is the possibility that our experiments may first detect decomposition products from molten RDX still constrained in a matrix of binder and still-solid RDX, while the other experiments mentioned above all sample gas primarily evolved from the surface of a liquid RDX layer. Under our conditions, steric effects might favor N-N bond breakage and NO₂ evolution. At the liquid/gas interface, on the other hand, RDX molecules may have the freedom of motion to execute more demanding reactions like detrimerization leading to N₂O formation. Our experiments also differ from those of the Brill group by using composite propellants rather than pure ingredients, from those of Behrens by having heating rates 3 to 4 orders of magnitude higher, and from those of the Litzinger group by monitoring a stationary observation volume towards which the burning surface moves, rather than moving a sampling probe into the gas stream produced by laser heating. The answer to the question posed by our apparent observations of earlier, slower evolution of NO₂ may lie in these differences, or in better understanding of our own experiments, and only further experiments will provide it.

In our earlier report we presented a review of the contributions by previous investigators to our understanding of the chemical mechanisms of RDX decomposition.² This body of work and our own experimental evidence continue to give a coherent picture which agrees with the prediction of Melius²⁶ that, on energetic grounds, RDX decomposition in the condensed phase will be dominated by processes involving N-NO₂ bond breaking, at least at high enough heating rates that catalytic processes are not important.

The dependence of processes and product distributions on heating rates is part of a more general dependence on the environment of the RDX molecule, including not only the temperatures and time scales involved but also the phase. The only experiments to date in which conditions clearly did not allow progress beyond the initial NO_2 loss step are the fast laser pyrolysis experiments of Botcher and Wight¹¹⁻¹³ (although with longer laser pulses they could observe formation of other products including N_2O). The experiments discussed earlier, including ours, cover in all five orders of magnitude in heating rate, with our experiments in the middle of the range. By examining Figure 14 (and comparing it with the N_2O , NO_2 , and NO mole fractions reported here), we can conclude that it is not easy to discern any systematic trends in product mole fractions, given that differences in observed concentrations are only at the factor of two level and that other differences in the experimental conditions can also easily generate differences at the same level.

Our observations of NO_2 are consistent with the above picture. Our heating rates are slow compared to chemical reaction rates, and even if HONO or other species are initial products, they

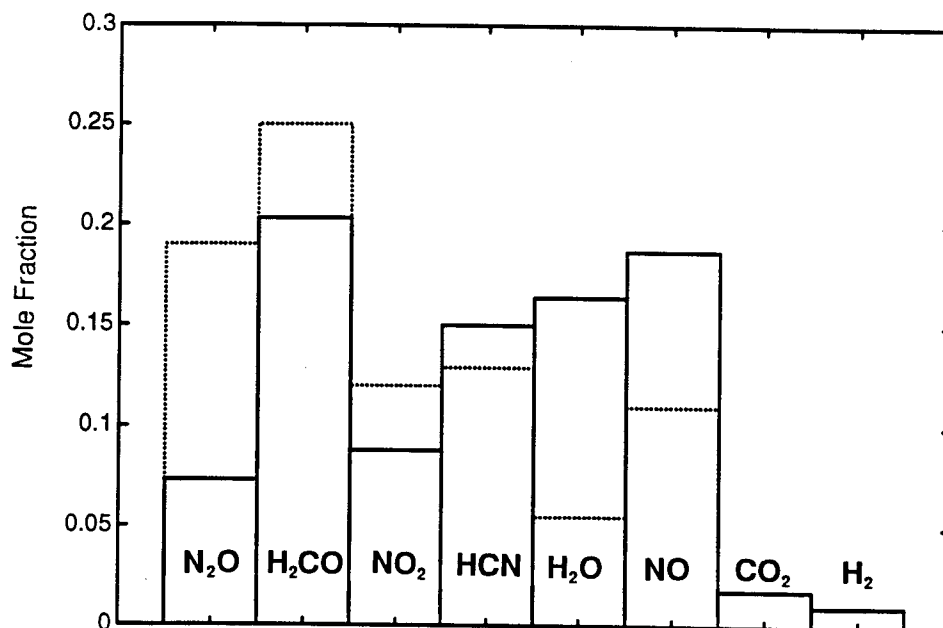


Figure 14. Major RDX Decomposition Gas Species Mole Fractions from Experiments of Fetherolf and Litzinger⁷⁻⁸ Compared to Adaptation of Observations of Behrens⁶ (dots).

originate in a mixed gas/liquid region with plenty of opportunity for homogeneous or heterogeneous reactions to carry initial products of decomposition to secondary products including the more stable NO_2 . On the other hand, transport of NO_2 , perhaps formed by some of the first bond-breaking processes in RDX, into our observation region would appear to be direct enough that much of it survives without reacting, dimerizing, or otherwise disappearing. Additional observations would help us be more confident about the time history of NO_2 appearance, and add to our understanding of the environment in the decomposition region and during transport through the propellant.

Finally, we turn to the question of NO formation mechanisms. Both gas phase and condensed phase candidates have been put forward. Brill has pointed out¹³ that secondary reactions among the products of the two global decomposition steps will provide the heat to sustain pyrolysis. Among these, both $\text{CH}_2\text{O} + \text{NO}_2$ and $\text{HCN} + \text{NO}_2$ will produce NO. In the condensed phase, on the other hand, the reaction of a nitrogen centered RDX radical (formed from N-N bond cleavage) with NO_2 to form the nitrite (rapidly decomposing to the nitroxide) and NO has been proposed.¹ The gas phase reactions will be fast, while the condensed phase reactions may require higher temperatures than NO_2 evolution, so in either case it would not be surprising if NO and N_2O appearance were indeed simultaneous, following NO_2 appearance. Our observations do not tell us that NO and N_2O appear simultaneously, of course, although the simplest assumption we can make about the separately observed abrupt appearances of NO and N_2O is that they are both associated with the same sudden connection of pressurized voids to the observation volume. Again, more simultaneous observations of more species would answer these questions.

6.0 SUMMARY

We draw two major conclusions from our work to date: N_2O , NO_2 , and NO are all observed as decomposition products of RDX embedded in binder under actual combustion conditions, and they are formed in high temperature regions of the condensed phase but are able to penetrate through cracks into regions of the propellant which are otherwise little affected by the advancing flame front. Our observations by themselves will of course not fully specify the structure of a strand near the burning surface and the physical mechanisms which shape it, but they certainly strongly encourage the speculation that the suddenly appearing decomposition gases originate in pressurized bubbles inside liquid RDX which in turn is contained inside a still solid matrix formed by the propellant binder. This matrix would have to be structurally sound enough that some bubbles are prevented from releasing their contents upward into the flame region, but instead eject decomposition gas into the observation volume when cracks open up into it. In our earlier work, a substantial body of observations of N_2O alone laid the groundwork for the above physical model. In the work covered by this report, additional observations of NO_2 and NO have raised very interesting questions stemming from their relative time histories, with the potential to provide important information for models of nitramine decomposition chemistry during the combustion of actual propellant formulations.

7.0 REFERENCES

1. J. Wormhoudt and P. L. Keabian, in Proceedings of the 30th JANNAF Combustion Subcommittee Meeting, CPIA Publication 606, Vol. II, pp. 329-338.
2. J. Wormhoudt, P. L. Keabian, and C. E. Kolb, "Infrared Fiber Optic Diagnostic Observations of Solid Propellant Combustion", Final Report for U. S. Army Research Office Contract DAAL03-91-0008, Aerodyne Research Report ARI-RR-1029, October 1993.
3. J. Wormhoudt, P. L. Keabian, and C. E. Kolb, submitted to *Combustion and Flame.*, 1994.
4. M. H. Alexander, P. J. Dagdigian, M. E. Jacox, C. E. Kolb, C. F. Melius, H. Rabitz, M. D. Smooke, and W. Tsang, *Prog. Energy Combust. Sci.* 17, 263 (1991).
5. G. F. Adams, and R. W. Shaw, Jr., *Ann. Rev. Phys. Chem.* 43, 311 (1992).
6. R. Behrens, Jr., and S. Bulusu, *J. Phys. Chem.* 96, 8877 (1992).
7. B.L. Fetherolf, and T.A. Litzinger, Proceedings of the 30th JANNAF Combustion Subcommittee Meeting, CPIA Publication No. 606, Vol. II, 1993, p. 15-31.
8. B.L. Fetherolf, T.A. Litzinger, Y.-C. Liu, and K. K. Kuo, Proceedings of the 30th JANNAF Combustion Subcommittee Meeting, CPIA Publication No. 606, Vol. II, 1993, p. 183-195.
9. J. Wormhoudt and P. L. Keabian, "Embedded Infrared Fiber Optic Absorption Studies of Nitramine Propellant Strand Burning", in Proceedings of the 31st JANNAF Combustion Subcommittee Meeting, October 1994, Chemical Propulsion Information Agency, Johns Hopkins University, to appear.
10. L.S. Rothman, R.R. Gamache, R.H. Tipping, C.P. Rinsland, M.A.H. Smith, D.C. Benner, V. Malathy Devi, J.-M. Flaud, C. Camy-Peyret, A. Perrin, A. Goldman, S.T. Massie, L.R. Brown and R.A. Toth, *J. Quant. Spectrosc. Radiat. Transf.* 48, pp. 469-507, 1992.
11. W. Schneider, G. K. Moortgat, G. S. Tyndall, and J. P. Burrows, *J. Photochem. and Photobiol.* 40, 195 (1987).
12. D. K. Hsu, Spectral Atlas of Nitrogen Dioxide, 5530 to 6480 Å, Academic Press, New York, 1978.
13. T. B. Brill, and P. J. Brush, *Phil. Trans. R. Soc. Lond. A* 339, 377 (1992).
14. C. F. Melius, *Phil. Trans. R. Soc. Lond. A* 339, 365 (1992).
15. C.A. Wight, and T. R. Botcher, *J. Am. Chem. Soc.* 114, 8303 (1992).

16. T.R. Botcher, and C.A. Wight, in Structure and Properties of Energetic Materials, (D. H. Liebenberg, R. W. Armstrong, and J. J. Gilman, Eds.), Materials Research Society, Pittsburgh, PA, 1993, Mat. Res. Soc. Symp. Proc. Vol. 296 , p. 47.
17. T.R. Botcher, and C.A. Wight, J. Phys. Chem. 97, 9149 (1993), and J. Phys. Chem. 98, 5441 (1994).

8.0 LIST OF PUBLICATIONS AND TECHNICAL REPORTS

"Infrared Fiber Optic Diagnostic Observations of Solid Propellant Combustion", J. Wormhoudt and P. L. Kebabian, submitted to Combustion and Flame (1994).

"Embedded Infrared Fiber Optic Absorption Studies of Nitramine Propellant Strand Burning", J. Wormhoudt and P. L. Kebabian, in Proceedings of the 31st JANNAF Combustion Subcommittee Meeting, October 1994, Chemical Propulsion Information Agency, Johns Hopkins University, to appear.

"Embedded Fiber Optic Studies of Nitramine Composite Strand Burning", J. Wormhoudt, P. L. Kebabian, and C. E. Kolb, to be submitted to Combustion and Flame (1994).

9.0 LIST OF PARTICIPATING SCIENTIFIC PERSONNEL

Dr. Joda Wormhoudt was the Principal Investigator for the project, assembling, performing, and analyzing the experiments. Dr. Paul Kebabian designed and implemented a series of upgrades to the experimental apparatus, and also assisted with test article assembly and observations. Dr. David Nelson modified data acquisition programs for both the NO₂ (HeNe absorption) and NO (tunable diode laser absorption) measurements. Dr. Mark Zahniser assisted in readying the tunable diode laser apparatus for our demonstration experiment. Dr. Charles E. Kolb participated in experimental planning and data analysis.

10.0 REPORT OF INVENTIONS

This project did not result in any inventions, and we do not anticipate any patent application based on contract work.